

Microbranching in mode-I fracture using large-scale simulations of amorphous and perturbed-lattice models

Shay I. Heizler^{1,2,*} and David A. Kessler^{1,†}

¹*Department of Physics, Bar-Ilan University, Ramat-Gan IL52900, Israel*

²*Department of Physics, Nuclear Research Center-Negev, P.O. Box 9001, Beer Sheva 84190, Israel*

(Received 29 March 2015; published 6 July 2015)

We study the high-velocity regime mode-I fracture instability wherein small microbranches start to appear near the main crack, using large-scale simulations. Some of the features of those microbranches have been reproduced qualitatively in smaller-scale studies [using $\mathcal{O}(10^4)$ atoms] on both a model of an amorphous material (via the continuous random network model) and using perturbed-lattice models. In this study, larger-scale simulations [$\mathcal{O}(10^6)$ atoms] were performed using multithreading computing on a GPU device, in order to achieve more physically realistic results. First, we find that the microbranching pattern appears to be converging with the lattice width. Second, the simulations reproduce the growth of the size of a microbranch as a function of the crack velocity, as well as the increase of the amplitude of the derivative of the electrical-resistance root-mean square with respect to the time as a function of the crack velocity. In addition, the simulations yield the correct branching angle of the microbranches, and the power law exponent governing the shape of the microbranches seems to be lower than unity, so that the side cracks turn over in the direction of propagation of the main crack as seen in experiment.

DOI: [10.1103/PhysRevE.92.012403](https://doi.org/10.1103/PhysRevE.92.012403)

PACS number(s): 62.20.mm, 46.50.+a

I. INTRODUCTION

The study of the physics of brittle fracture has been very fruitful in the past two decades [1–3]. New experiments have shown various new features of dynamic fracture, focused on Mode-I (tensile) fracture in amorphous brittle materials [4–7]. In particular, the experiments have shown a sharp transition between the regime of steady-state cracks and the regime of unstable cracks [5,6]. In steady state, where the driving displacement, Δ (of order Δ_G , the Griffith criterion), is sufficiently small, a single crack propagates along the midline of the sample, reaching a steady-state velocity (which is of the order of the Rayleigh surface wave speed, c_R). Increasing Δ results in an increased steady-state velocity, yielding a $v(\Delta)$ curve, until a specific critical point. Increasing the driving displacement further, beyond this critical point, we enter the unstable regime, where small microbranches start to appear nearby the main crack. The experiments have shown that above the critical point, the size of the average microbranch (which is log-normal distributed) increases rapidly with the crack velocity, as measured via the slope of the electrical resistance of a conductive layer that is pasted on the sample. The electrical resistance slope exhibits oscillations whose amplitude increases rapidly as well. Increasing the driving displacement further, the small microbranches become large microbranches, generating a complex fracture pattern, and finally, creating macrobranches [1,6,8].

Some of the new experimental findings could not be explained via the classical theoretical approach for fracture mechanics, the linear elasticity fracture mechanics (LEFM) theory [9]. For example, several predictions of LEFM for the critical velocity, such as the studies of Yoffe [10] or Eshelby [11] predicted a single universal critical velocity much higher than that seen in some of the experimental studies,

such as in PMMA [1]. Also, experiments have found various material-dependent features such as the terminal velocity, at which the crack manages to propagate, as well as the critical velocity for macrobranches [1]. In regard to the microbranching critical velocity, the question of universality is debatable [12], but at any rate, the velocities are much smaller than the theoretical predictions. For a review, see the Introduction in Ref. [13]. However, the basic reason for the failures of LEFM is that the basic equations of LEFM yield a singularity of the stresses near the crack tip [9], and thus, the zone nearest to the crack's tip (the process zone) cannot be modeled via LEFM.

The failure of LEFM, caused by this singularity, gave rise to an interest in discrete lattice models and simulations [14–23]. In this kind of model, the basic length-scale, which is the lattice scale, prevents the singularities that appear in the continuum approach. The lattice models were successful in reproducing the behavior of steady-state cracks [14,15,17], including a material dependency of the $v(\Delta)$ curves, in that it depends on the specific parameters of the interatomic potential [20,21]. Moreover, the lattice models predict a certain critical point beyond which the steady-state solution becomes linearly unstable [18–21]. In the simulations, this is exactly the point which the crack stops propagating along the midline of the sample and some additional bonds, not along the midline, start to break [16,18,20,24]. However, especially in mode-I pure lattice simulations, the postinstability behavior of the lattice models do not match the experiments, neither quantitatively nor qualitatively [20,24].

One recent approach to overcome these difficulties has been to turn to a more realistic model for an amorphous material, the continuous random network (CRN) model [25]. The continuous random network was suggested first by Zachariassen for describing amorphous materials [26], and specific effective algorithms (using Monte Carlo techniques) for generating the CRN were offered in Refs. [25,27,28]. Recent accurate 2D experiments using transmission electron microscopy (TEM) in 2D silica on the structure of this

*highzlers@walla.co.il

†kessler@dave.ph.biu.ac.il

amorphous material were reproduced to excellent accuracy using the Zachariassen model [29,30]. After generating an amorphous CRN sample, molecular dynamics simulations were found to yield many of the important qualitative features of mode-I fracture experiments in amorphous brittle materials [25]. The simulations showed the birth of microbranches growing nearby the main crack, the increase of the size of the microbranches as a function of the driving displacement (or of course, the crack velocity), and the growth of the amplitude of the derivative of the electrical resistance with respect to the time as a function of the crack velocity.

Another direction recently examined was that of perturbed-lattice models [13], which exhibited behavior similar to that of the CRN model, including the main features mentioned above. However, these simulations (both the CRN and the perturbed-lattice simulations) suffered from a significant level of numerical noise, since each microbranch contained only a few tens of broken bonds at most. Thus, the statistics that concerns the most interesting physics, that of the branches, was quite poor.

These intriguing results, performed on limited-size systems [$\mathcal{O}(5 \times 10^4)$ atoms] provide strong motivation to conduct larger simulations both to reduce the overall noise level and to get closer to at least a mesoscopic system where scaling behavior might set in. The goal was to achieve at least a two-magnitude increase in size, i.e., simulations of the order of millions of atoms [$\mathcal{O}(5 \times 10^6)$ atoms], which necessitated using parallel (multithreading) computing. In this work we study mode-I fracture via large-scale simulations, with a particular focus on the properties of the microbranches that could not be studied in the previous, limited-size studies. In addition, recently experiments have been performed with gels, whose three orders of magnitude slower sound speed (compared to the classic brittle materials like PMMA or glass) enables direct visualization by means of moderately fast video cameras, resulting in clear snapshots of the crack tip [3,7,31]. Using the larger-scale simulations we can now compare the crack's tip shape, both on steady-state cracks in a strip geometry and, especially, near the origin of the microbranching instability.

The models are presented in Sec. II. In Sec. III we perform some basic checks of our models, confirming that the transverse size of the microbranch zone ($\delta y/W$) decreases with increasing sample width W , for a given scaled driving displacement Δ/Δ_G (in the experiments, using macroscopic sample sizes, the microbranching region width is much smaller than the sample width and the dynamics of the fracture is not affected by the sample edges). Next, in Sec. IV we present the quantitative results concerning the birth and the growth of the microbranches and their physical features. A short discussion is presented in Sec. V.

II. MODEL AND MAIN METHODOLOGY

The simulations presented in this study are divided generally into two kinds. The first one uses the continuous random network (CRN) model (to model an amorphous material), and the second employs a perturbed honeycomb- or perturbed-hexagonal-lattice model. Both kinds of model were described in depth in Refs. [25] and [13], respectively. We will review them here shortly.

The CRN model reproduces various structural features of real brittle amorphous materials (though 2D, in this study) such as amorphous silicon or silica [29,30,32], and a 3D-extension of this model should reproduce the real behavior of fracture. The perturbed honeycomb lattice is the ordered phase of the CRN, as discussed at length in Ref. [13], and shares similar features and results (though with less noise). In addition, in Refs. [29,30] there is clear experimental 2D evidence that 2D ordered materials share the structural features of the perturbed honeycomb lattice. Also, the perturbed hexagonal lattice is a generalization of the hexagonal lattice that was used in many studies to study dynamic fracture (for example, see Refs. [1,16,23]), and facilitates comparison with this body of work.

1. Generating the continuous random network for modeling amorphous material

We generated two-dimensional CRNs by a 2D-analogue [25] of the WWW algorithm [27,28]. The potential that was used in the construction of the CRN included both a two-body central force and a three-body bond-bending force [33,34]:

$$E_{\text{tot}} = \sum_{i=1}^n \left[\sum_{j \in \mathcal{N}(i)} \frac{1}{4} k_r (|\vec{r}_{ij}| - a_{i,j}^2) + \sum_{j,k \in \mathcal{N}(i)} \frac{1}{2} k_\theta (\cos \theta_{i,(j,k)} - \cos \theta_C)^2 \right], \quad (1)$$

where $|\vec{r}_{ij}|$ is the radial distance between each pair of nearest-neighbor atoms and $a_{i,j} = a = 4$ is a constant lattice scale (in contrast to the perturbed-lattice model). k_r and k_θ are the radial and the azimuthal (three-body) spring constants, respectively. $\cos \theta_{i,(j,k)}$ is the cosine of the angles between each set of three neighboring atoms, defined of course by

$$\cos \theta_{i,j,k} = \frac{\vec{r}_{i,j} \cdot \vec{r}_{i,k}}{|\vec{r}_{i,j}| |\vec{r}_{i,k}|}, \quad (2)$$

where i is the central atom and (j,k) are its two neighbors. $\theta_C = 2\pi/3$ (characterizing a honeycomb lattice). We start from a pure honeycomb lattice, randomize large number of bonds, and perform a Monte Carlo procedure, wherein each cycle we switch two bonds, calculating the optimal positions of the atoms in the near zone of the switched bonds to determine the change of energy so as to decide whether to accept the switch. Finally, we get a CRN that looks like Zachariassen's patterns [25,26] and the TEM snapshots of the 2D amorphous Silica [29,30]. For a in-depth discussion, see Ref. [25].

2. Generating the perturbed lattice

Here we start with a perfect honeycomb or hexagonal lattice and randomize the lattice scale of each "bond," $a_{i,j}$:

$$a_{i,j} = (1 + \epsilon_{i,j})a, \quad i = 1, 2, \dots, n_{\text{atoms}}, \quad j \in \mathcal{N}(i), \quad (3)$$

where $\epsilon_{i,j} \in [-b, b]$, and b is constant for a given lattice, and in this work ranges between $0 \leq b \leq 0.1$, $a = 4$. $\mathcal{N}(i)$ refers to the nearest neighbors of site i . For a detailed discussion, see Ref. [13].

3. The equations of motion

In our model, between each two atoms there is a piecewise linear radial force (two-body force law) of the form

$$\vec{f}_{i,j}^r = k_r k'_{i,j} (|\vec{r}_{i,j}| - a_{i,j}) \hat{r}_{j,i}, \quad (4)$$

where

$$k'_{i,j} \equiv \theta_H(\varepsilon - |\vec{r}_{i,j}|). \quad (5)$$

The Heaviside step function θ_H guarantees that the force drops immediately to zero when the distance between two atoms $|\vec{r}_{i,j}|$ reaches a certain value $\varepsilon > a_{i,j}$ (the breaking of a “bond”). In this work we set $\varepsilon = a + 1$. We describe here brittle materials with an extremely sharp transition from linear response to failure, though in reality the failure is always somewhat smoother. Alternatively, we can replace Eq. (5) with a smoother force law, which instead of a sharp failure at $|\vec{r}_{i,j}| = \varepsilon$, has a more realistic smooth transition, wherein the force law drops to zero according to [18,20,21]:

$$k'_{i,j} \equiv \frac{1 + \tanh[\alpha_{\text{pot}}(\varepsilon - |\vec{r}_{i,j}|)]}{1 + \tanh(\alpha_{\text{pot}})}, \quad (6)$$

where α_{pot} is the smoothness parameter, such that when $\alpha_{\text{pot}} \rightarrow \infty$ the force law reverts to the piecewise linear force law. The effect of α_{pot} on the fracture feature was investigated previously [18,20,21] and is reproduced in this paper. The results in this paper refer to the piecewise linear model, unless mentioned otherwise.

In addition there is a three-body force law that depends on the cosine of each of the angles, acts on the central atom (atom i) of each angle, and may be expressed as

$$\begin{aligned} \vec{f}_{i,(j,k)}^\theta &= k_\theta (\cos \theta_{i,j,k} - \cos \theta_C) \frac{\partial \cos \theta_{i,j,k}}{\partial \vec{r}_i} k'_{i,j} k'_{i,k} \hat{r}_i \\ &= k_\theta (\cos \theta_{i,j,k} - \cos \theta_C) \left[\frac{\vec{r}_{i,j} + \vec{r}_{i,k}}{|\vec{r}_{i,j}| |\vec{r}_{i,k}|} + \frac{\vec{r}_{j,i} (\vec{r}_{i,j} \cdot \vec{r}_{i,k})}{|\vec{r}_{i,j}|^3 |\vec{r}_{i,k}|} \right. \\ &\quad \left. + \frac{\vec{r}_{k,i} (\vec{r}_{i,j} \cdot \vec{r}_{i,k})}{|\vec{r}_{i,j}| |\vec{r}_{i,k}|^3} \right] k'_{i,j} k'_{i,k}, \end{aligned} \quad (7)$$

while the force that is applied on the other two atoms (atoms j, k) may be expressed as

$$\begin{aligned} \vec{f}_{j,(i,k)}^\theta &= k_\theta (\cos \theta_{i,j,k} - \cos \theta_C) \frac{\partial \cos \theta_{i,j,k}}{\partial \vec{r}_j} k'_{i,j} k'_{i,k} \hat{r}_j \\ &= k_\theta (\cos \theta_{i,j,k} - \cos \theta_C) \left[\frac{\vec{r}_{k,i}}{|\vec{r}_{i,j}| |\vec{r}_{i,k}|} \right. \\ &\quad \left. + \frac{\vec{r}_{i,j} (\vec{r}_{i,j} \cdot \vec{r}_{i,k})}{|\vec{r}_{i,j}|^3 |\vec{r}_{i,k}|} \right] k'_{i,j} k'_{i,k}. \end{aligned} \quad (8)$$

Of course, the forces satisfy the relation $\vec{f}_{i,(j,k)}^\theta = -[\vec{f}_{j,(i,k)}^\theta + \vec{f}_{k,(i,j)}^\theta]$. The three-body force law drops immediately to zero when using a piecewise linear force law when the bond breaks [Eq. (5)], or may be taken to vanish smoothly, using Eq. (6). In a honeycomb lattice there are three angles associated with each atom and in the hexagonal lattice there are six of them (we note that in the hexagonal lattice this choice is a little bit arbitrary since there are in general additional optional angles for each atom). There is a certain preferred angle θ_C for which

the three-body force law vanishes (in the honeycomb lattice we set $\theta_C = 2\pi/3$ and in the hexagonal lattice we set $\theta_C = \pi/3$).

In addition, it is convenient to add a small Kelvin-type viscoelastic force proportional to the relative velocity between the two atoms of the bond $\vec{v}_{i,j}$ [17–20]:

$$\vec{g}_{i,j}^r = \eta (\vec{v}_{i,j} \cdot \hat{r}_{i,j}) k'_{i,j} \hat{r}_{i,j}, \quad (9)$$

with η the viscosity parameter. The viscous force also vanishes after the bond is broken, governed by $k'_{i,j}$. The imposition of a small amount of such a viscosity acts to stabilize the system and is especially useful in the relatively narrow systems simulated herein.

The set of equations of motion of each atom is then

$$m_i \vec{a}_i = \sum_{j \in 3p \text{ nn}} (\vec{f}_{i,j}^r + \vec{g}_{i,j}^r) + \sum_{j,k \in 3p \text{ nn}} \vec{f}_{i,(j,k)}^\theta + \sum_{j \in 6p \text{ nn}} \vec{f}_{j,(i,k)}^\theta, \quad (10)$$

when $p = 1$ for honeycomb lattice and $p = 2$ for hexagonal lattice. In this work the units are chosen so that the radial spring constant k_r and the atoms' mass m_i is unity. We note that numerical measurement of the Young's modulus of the hexagonal lattices for $k_\theta = 0$ yields the well-known analytical expression $E = 2/\sqrt{3}k_r$ and is twice as big ($E \approx 2k_r$) with $k_\theta/k_r = 10$. The Poisson's ratio is $\nu = 1/3$ as reported in many previous works [35,36]. In the honeycomb lattice and the CRN (with $k_\theta/k_r = 1$), the Young's modulus is approximately $E \approx 0.86k_r$, while the Poisson's ratio remains similar. However, the value of k_r is not crucial (in this study), since the results in this paper are in normalized units ($\Delta/\Delta_G, \nu/c_R$).

After relaxing the initial lattice, we strain the lattice under a mode-I tensile loading with a given constant strain corresponding to a given driving displacement $\pm \Delta$ of the edges (the top and bottom rows are held tight and do not allow transverse displacement) and seed the system with an initial crack (the left boundary condition is also held in a pure “cracked” state). The crack then propagates via the same molecular dynamics Euler scheme using Eqs. (4)–(10). We note that the calculation of Δ_G is obtained by equating of the energy in the uncracked uniform strain to the energy needed for breaking the midline bonds in the sample (for example, see Ref. [17] for the case of square lattice). We parametrize our results in this paper using the normalized quantity Δ/Δ_G , but of course $\Delta/\Delta_G = K_I/K_{IC}$ (the stress intensity factor normalized to the Griffith value) [1].

4. Parallelization by GPU computing

As mentioned in the Introduction, the major innovation of this work, compared to our previous studies, is the use of large-scale simulations. The previous studies of the amorphous (CRN) model [25] and the perturbed-lattice model [13] used approximately 50 000 particles. In this study we wished to use approximately 5 000 000 particles. These kind of simulations cannot reasonably be performed by a single CPU, and we are forced to use multithread computing. We chose to use GPU computing, parallelizing the code via CUDA [37,38]. This kind of programming obliges the programmer to use the different levels of memory carefully [38], in order to make

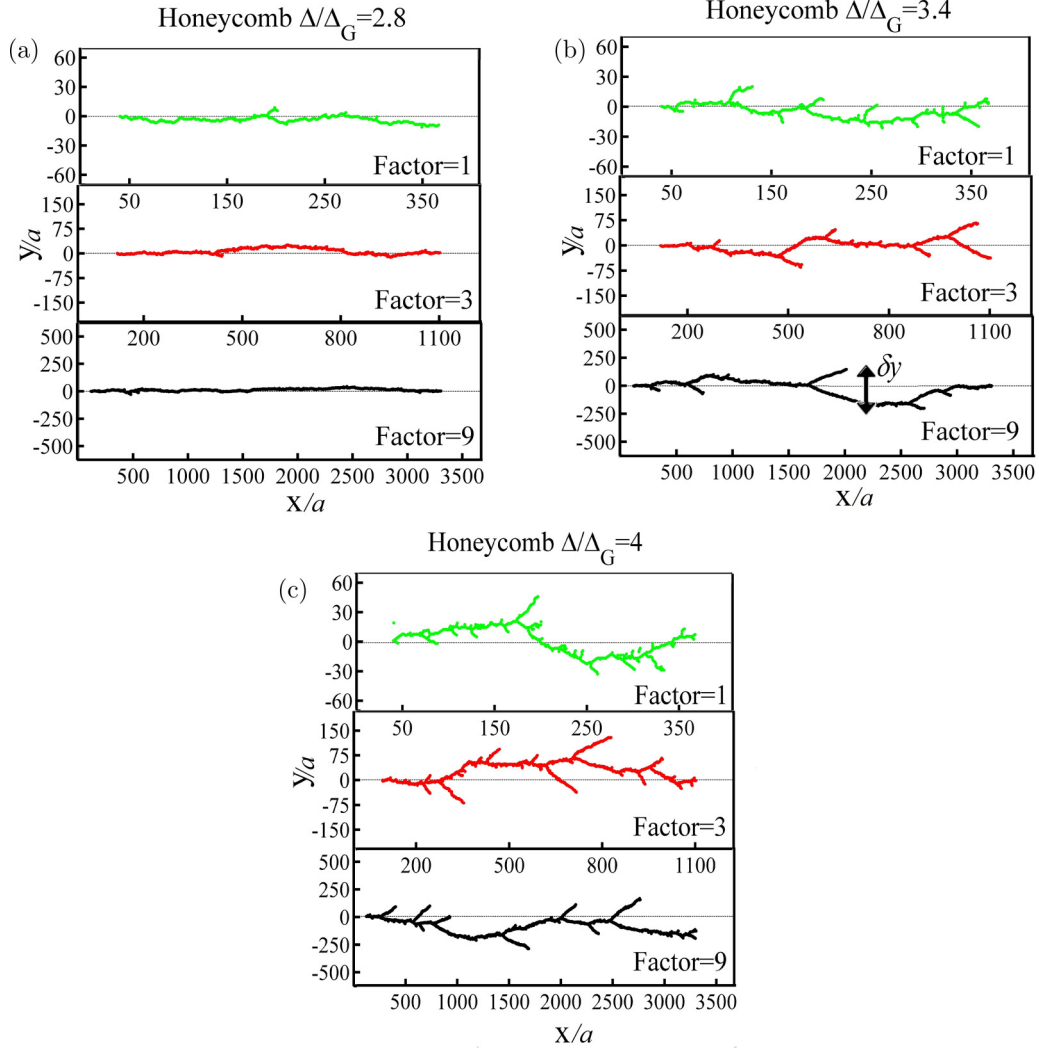


FIG. 1. (Color online) (a) The microbranching pattern in a perturbed honeycomb lattice for $\Delta/\Delta_G = 2.8$ and $\eta = 2$ for $f = 1$ in the upper curve, for $f = 3$ in the intermediate curve, and for $f = 9$ in the lower curve. x and y have the units of a , the lattice scale, and each figure depicts the whole sample (except for the the initial seed crack that extends from the left edge of each crack pattern to $x = y = 0$). (b) The same for $\Delta/\Delta_G = 3.4$. (c) The same for $\Delta/\Delta_G = 4.0$. In (b) we define δy , the width of the microbranching region, as the difference between the maximum and minimum y 's of broken bonds.

possible the achieving of an acceleration up to ≈ 100 faster than a regular C code using a single CPU. Beside the benefit of getting the results in a given system much faster, the main benefit is the possibility to run large-scale simulations, which was prohibitive before. This tool makes possible the simulation of millions of atoms in reasonable simulation times.

Our model consists of several modules, each one of which needs to be rewritten in CUDA. Both amorphous and lattice models use a molecular-dynamics module for the fracture simulations that must be parallelized. In addition, for the CRN, the Metropolis Monte Carlo algorithm for generating the CRN needs to be parallelized. Furthermore, the electrical resistance simulations, which we use to determine the crack velocity [25], is solved by a nonlinear Laplace solver that needs to be parallelized too. The electrical resistance is calculated via the method that was used in Ref. [25], by solving the nonlinear Laplace equation on a grid of resistors (each broken bond, in the main crack and in the microbranches, is taken into account) [39]. In Appendix A we discuss the implementation

of the different modules, the parameters that were used, and the degree of acceleration achieved for the different modules with the GPU using CUDA.

The various sized lattices we use contain:

(1) $162 \times 272 \approx 45\,000$ ($N = 80$ in the Slepian model notation) atoms for the honeycomb lattice and $162 \times 408 \approx 65\,000$ atoms for the hexagonal lattice, which we call $f = 1$ (Factor = 1). This size is equal to that used in our previous studies, Refs. [25] and [13].

(2) $486 \times 816 \approx 400\,000$ ($N = 240$ in the Slepian model notation) atoms for the honeycomb lattice and $486 \times 1224 \approx 600\,000$ atoms for the hexagonal lattice, which we call $f = 3$ (Factor = 3).

(3) $1458 \times 2448 \approx 3\,600\,000$ ($N = 720$ in the Slepian model notation) atoms for the honeycomb lattice and $1296 \times 3264 \approx 4\,200\,000$ ($N = 640$ in the Slepian model notation) atoms for the hexagonal lattice, which we call $f = 8-9$ (Factor = 9 in the honeycomb and CRN lattices and Factor = 8 in the hexagonal lattice).

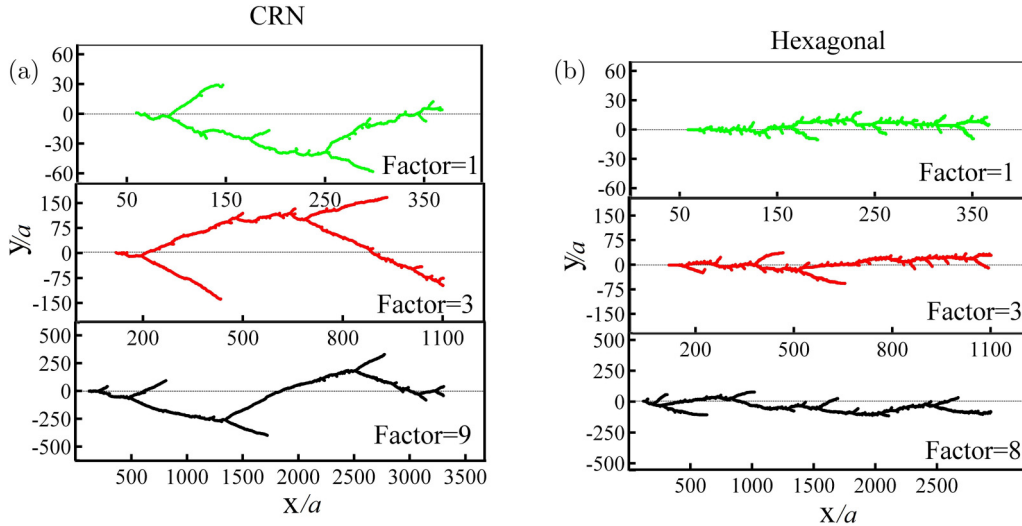


FIG. 2. (Color online) (a) The microbranching pattern using the continuous random network (CRN) model for $\Delta/\Delta_G = 3.6$ and $\eta = 2$ for $f = 1$ in the upper curve, for $f = 3$ in the intermediate curve, and for $f = 9$ in the lower curve for continuous random network (CRN) model. (b) The same for perturbed hexagonal lattice for $\Delta/\Delta_G = 1.7$ and $\eta = 0.25$.

In Appendix B we present a brief discussion regarding the results for the CRN using the parallel GPU Monte Carlo algorithm. The GPU algorithm reproduced the results of the CPU code, in particular the agreement [25] of the radial distribution function with that experimentally determined [32] for amorphous silicon.

III. OVERVIEW OF THE SIMULATION RESULTS

In Figs. 1(a)–1(c) we present the fracture pattern of the broken bonds for the small-size perturbed honeycomb lattice (that was used before in Ref. [13], called here $f = 1$), for the intermediate size lattice ($f = 3$), and for the large lattice ($f = 9$), for three values of the driving displacement: small ($\Delta/\Delta_G = 2.8$), intermediate ($\Delta/\Delta_G = 3.4$), and large ($\Delta/\Delta_G = 4$). The fracture patterns are plotted in the x - y plane and depict the full simulated sample, where x and y have the units of a , the lattice scale. In the large driving simulation for $f = 1$ reported upon in our previous work, the microbranches reached the edge of the sample. In addition, in Fig. 2(a) we present fracture patterns using the amorphous CRN model (that was used before in Ref. [25]) with $\Delta/\Delta_G = 3.6$ for the different sizes of lattices, and in Fig. 2(b), fracture patterns using a perturbed hexagonal lattice.

In the figures we can immediately see the benefit of the larger-scale simulations; the noisy fracture patterns that were obtained using $f = 1$ (the upper pattern in each figure) transform to the smoother and more physical-like patterns at $f = 8$ –9. In Fig. 2(b) we can see clearly the curved power-law shape of the microbranches (for a quantitative discussion, see Sec. IV C).

A closer look reveals an important point: For a given driving displacement, the relative width of the fracture pattern decreases with the increase of the lattice size. This is crucial since otherwise the branching pattern in a macroscopic material would be macroscopic as well, against the evidence of

the experiments [5]. In Fig. 3, we can see the relative fracture zone width $\delta y/W$, when δy is the width of the microbranching pattern [see Fig. 1(b) for a pictorial explanation], defined as the difference between the maximum and minimum y 's of broken bonds, and W is the sample width. For any given value of Δ/Δ_G the normalized width of the microbranching pattern decreases with the lattice width. This effect is seen clearly in the perturbed honeycomb lattice and in the CRN lattice, and in a more moderate way in the hexagonal perturbed lattice. This result is crucial; if the lattice models are physical, then when increasing the lattice size, the relative fracture zone must decrease, so that the branching does not remain macroscopic in the $N \rightarrow \infty$ limit, which would conflict with the experimental results. It can be seen that the dependence of δy on Δ is more or less linear. This may be related to the linear increase of the size of the average microbranch as a function of the driving displacement [for example, see Fig. 8(b) below].

IV. RESULTS

A. The crack's tip shape

As mentioned in the introduction, the new experiments using gels yield clear snapshots of the crack tip [3,7,31]. Larger scale simulation enable us to compare the crack-tip shape to the experimental snapshots in both steady-state cracks and near the origin of instability.

First, we present the very good agreement between experiment and simulations of the crack's tip shape in steady-state cracks in the finite-width strip geometry in Fig. 4. In the upper picture, when the crack length is small comparing to the sample's width, the crack has the (well-known) parabolic shape; no blunting can be seen and LEFM works perfectly (except for nonlinear effects in the extreme crack-tip zone [7]). As the crack length grows, the finite width of the strip affects the crack's tip shape, generating a "tadpole-like" shape. We performed lattice simulations in a finite-width strip using

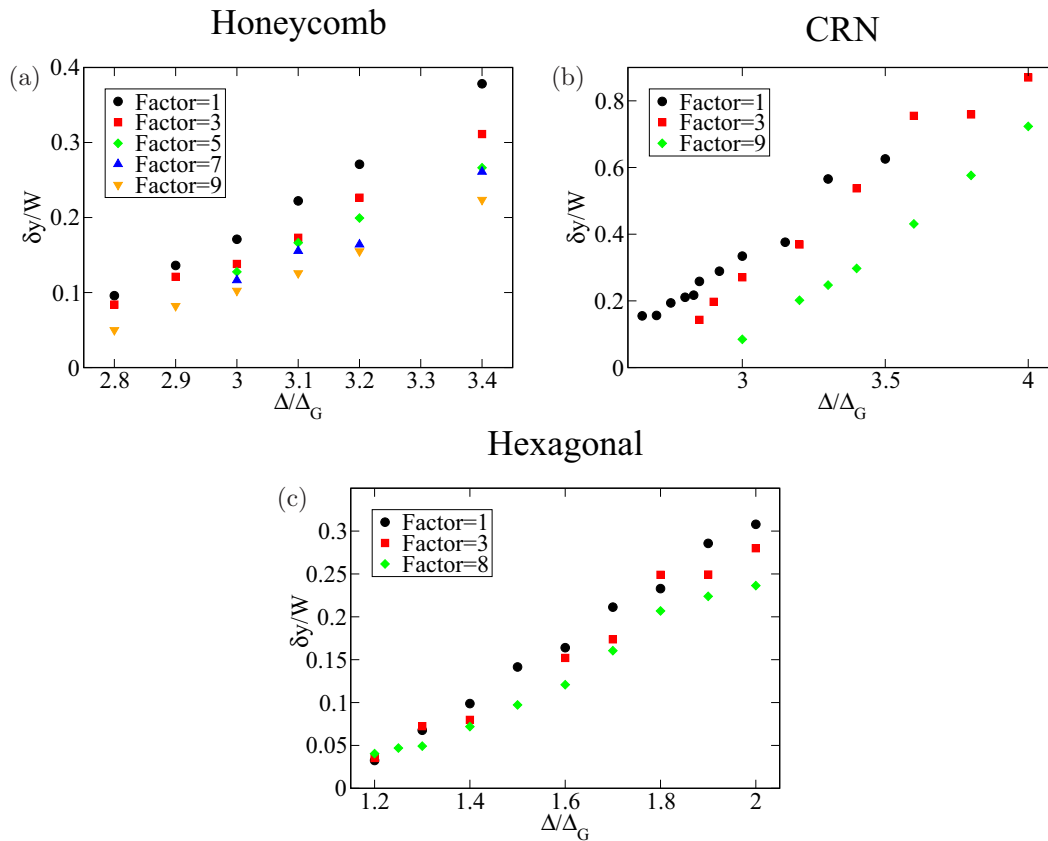


FIG. 3. (Color online) (a) The scaled width of the microbranching pattern $\delta y/W$ for (a) a honeycomb perturbed lattice, (b) the CRN model, and (c) a hexagonal perturbed lattice, for different lattice sizes.

different values of Δ/Δ_G . Since the simulations have only a finite number of atoms, the results are scaled to the real size of the experimental sample. We can see in Fig. 4 the excellent match of the crack’s tip shape between pure lattice simulations (described in detail below) and the experiments. This “tadpole”

shape is generic for finite-size (strip) lattice simulations, both honeycomb or hexagonal, with any amount of viscosity. Since the experimental crack is not exactly symmetric between the upper and the lower size of the crack, we used several values of Δ/Δ_G to get an optimal match between experiment and simulation (the small Δ/Δ_G shape is somewhat better on the upper side and the large Δ/Δ_G shape is somewhat better in the lower side).

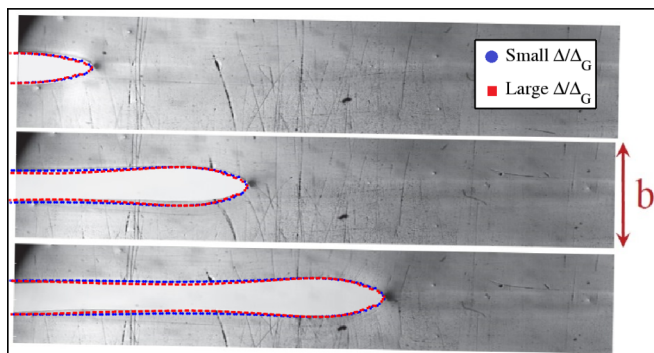


FIG. 4. (Color online) Several snapshots of the crack’s tip in steady-state mode-I fracture in experiments on gels. In the upper picture, when the crack length is small comparing to the sample’s width, the crack has the (well-known) parabolic shape. As the crack length grows, the finite size of the strip effects the crack’s tip shape, generating a “tadpole-like” shape. The lattice simulations for the crack-tip shape are added to the snapshots in the dashed curves. The experimental pictures are taken from Ref. [3].

Moreover, in Ref. [3] there are snapshots of the crack-tip shape near the origin of the microbranching instability (on the right-hand side of Fig. 5). In order to reproduce this crack-tip shape (in addition to using the large-scale simulation), we set $\varepsilon = 2a$ (only for this part in the paper), to magnify the crack-tip radius compared to the lattice scale a . This enables us to meaningfully compare the simulation results to experiments (this value of ε is a bit extreme, but qualitatively, the same physical effect can be seen using smaller values of ε). The lattice simulations are presented on the left-hand side of Fig. 5.

We can see that there is a close resemblance between the two series of snapshots. At first, the crack travels in the midline of the sample, yielding the parabolic crack tip shape of LEFM. When a new microbranch is born, the crack tip bifurcates into two, while very rapidly one “wins” and continues to propagate, and the other “dies.” The branch that continues to propagate has a slightly deformed shape compared to its original shape before it continues to propagate (the crack shape here significantly differs from the LEFM prediction). All of

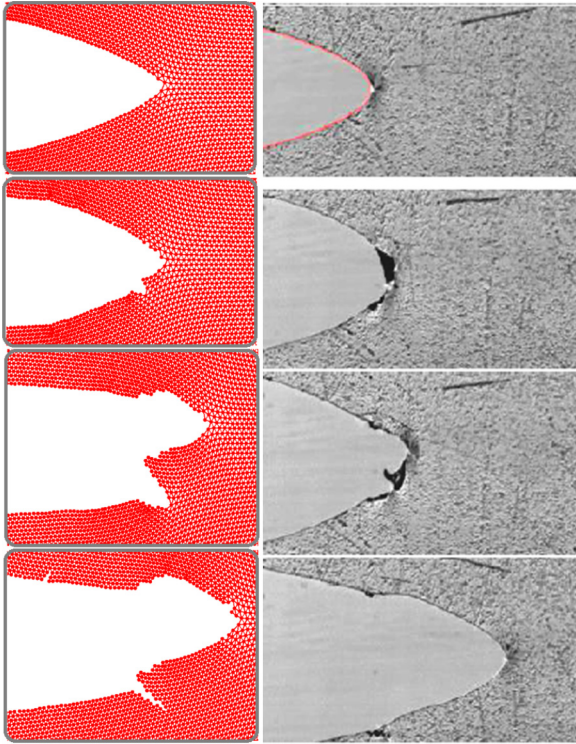


FIG. 5. (Color online) Several snapshots of the crack tip near the origin of the microbranching instability. On the right, there is a series of experimental snapshots of the crack tip before, during, and right after a new microbranch is born. On the left, there is a series of snapshots of our lattice simulations. Qualitatively, there is a very close resemblance between the two series. The experimental pictures are taken from Ref. [3].

these features are reproduced in the lattice simulations. It is important to mention that both experiments and simulations reveal that the origin of microbranching in mode-I fracture always lies in the immediate vicinity of the crack tip itself, rather than far behind the main crack.

B. Length of microbranches

In this section we present the quantitative results for various features of the fracture patterns, especially the microbranches. First, we present the $v(\Delta)$ curve, the total amount of broken bonds in the microbranches, measured for a crack that reached the end of the strip, as a function of the crack velocity and the root-mean square (RMS) of $dR(t)/dt$, the rate of increase of the derivative of the electrical resistance with respect to time as a function of the crack velocity. The results are normalized to c_R , the Rayleigh wave speed, which is calculated for different values of k_θ in Appendix C. The results for the perturbed honeycomb lattice is presented in Fig. 6, for the CRN in Fig. 7 and for the perturbed hexagonal lattice in Fig. 8.

We can clearly see that in all three models the slope of the $v(\Delta)$ appears to saturate in the high-velocity regime for the larger system sizes. This saturation is known from previous lattice studies [20]. The shape of the curves are similar to the experimental $v(\Delta)$ curves of real amorphous materials [1]. A close look at the curves of the total amount of broken bonds in the microbranches (which is our proxy for the average length of a microbranch as measured experimentally, which we use to reduce the statistical noise) as a function of the crack velocity, using both the honeycomb perturbed lattice and the CRN, reveals quantitatively what we have seen qualitatively using small-system sizes. Due to the noisiness of using finite-size

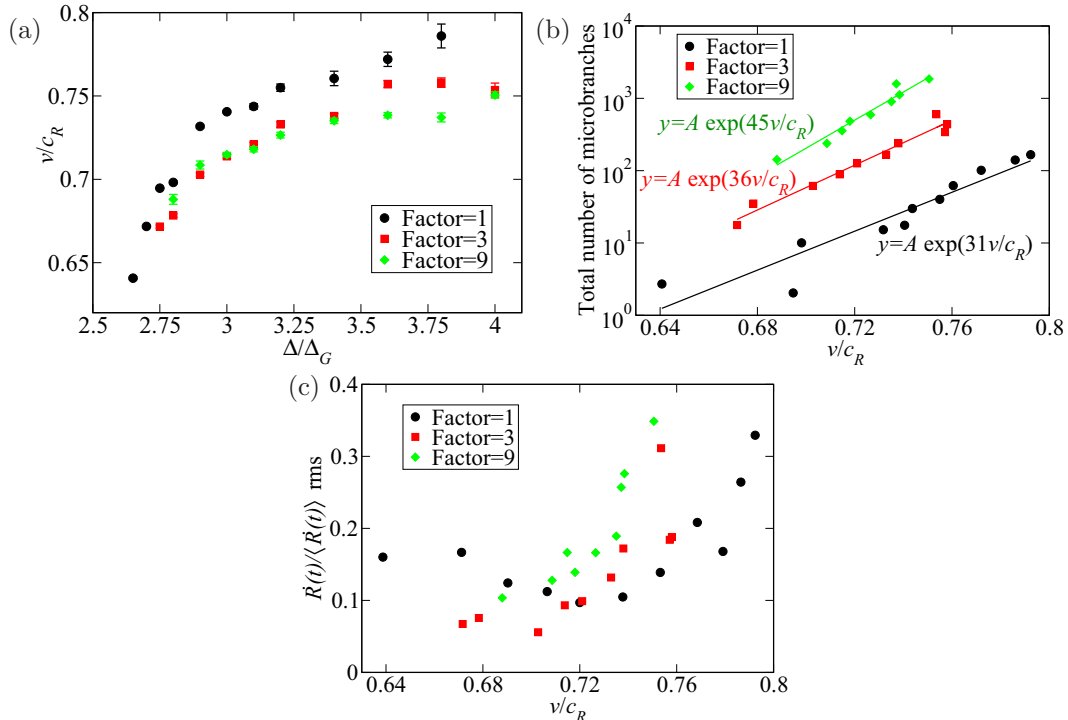


FIG. 6. (Color online) (a) The $v(\Delta)$ curve of a perturbed honeycomb lattice using different lattice sizes. (b) Total number of broken bonds in the microbranches as a function of the crack velocity. (c) The root-mean square of the derivative of electrical resistance with respect to the time as a function of the crack velocity.

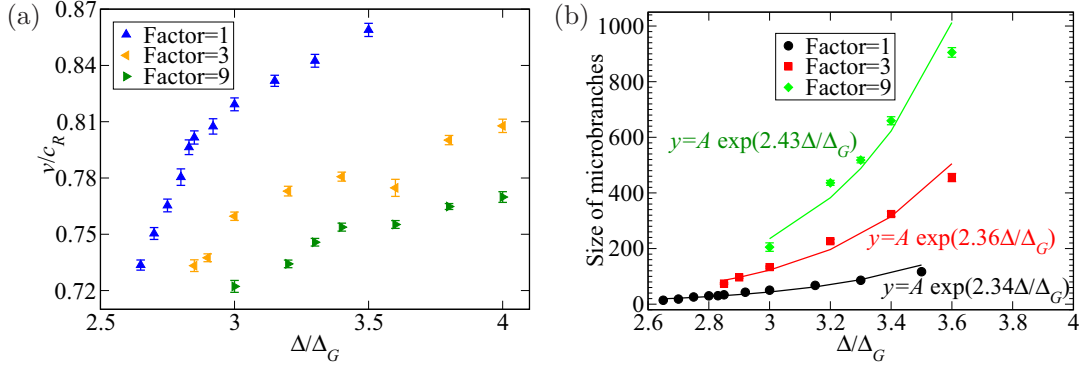


FIG. 7. (Color online) (a) The $v(\Delta)$ curve of a CRN lattice using different lattice sizes. (b) Total amount of broken bonds in microbranches as a function of the crack velocity.

lattices, rather than two different regimes, with a single steady-state crack at small velocities, and a sharp increase in the length of a microbranch in the large-velocity regime, we get a smooth exponential behavior. However, the exponent of the curves increases robustly with the lattice size, sharpening the difference between the steady-state regime and the microbranching (large-velocity) regime. In addition we can see that, in general, the CRN results act like a very perturbed honeycomb lattice, i.e., for any given Δ/Δ_G , the number of broken bonds is larger in the CRN than in the perturbed honeycomb lattice, similar to what we saw in Ref. [13]. In addition, using the honeycomb perturbed lattice we can see the increase of the RMS amplitude of the derivative of the electrical resistance with respect to the time as a function of the crack velocity. At high velocities, the RMS amplitude is approximately three times greater than the amplitude at low crack velocities, in agreement with the experiments regarding the RMS of the crack velocity [Fig. 11(c) in Ref. [5]].

Looking at the results for the perturbed hexagonal lattice, we get one of the most important results of this paper. In Fig. 8(b), we present the normalized number of microbranch broken bonds (per number of bonds in the entire system) as a function of the crack velocity. The different curves (using various lattice size) are similar to each other; however, enlarging the lattice size, the transition becomes sharper with f . Using $f = 8$, we can see two different separate regimes (one of steady-state cracks and one for

microbranching), that looks very much like the transition of the average microbranch length in the experiments [Fig. 11(a) in Ref. [5]]. This result verifies the main assumption of the lattice models. The physical phenomena of microbranching is qualitatively described by lattice models and simulations; when enlarging the system size, the results become more quantitatively similar to the (macroscopic) experimental results.

Nevertheless, quantitatively, the critical velocity that was found in the experiments was less than the critical velocities that were seen in our simulations. However, in previous studies it was shown that in the lattice models, we can control the critical velocity using different values of α_{pot} [20,21]. Here we check that this is still valid when using a three-body force law and a perturbed lattice. In Fig. 9(a), for the case $f = 1$, we present the total amount of microbranches using the perturbed honeycomb lattice. We can see that, first, $\alpha_{pot} = 1000$ reproduces the piecewise linear results, as expected. Second, smaller values of α_{pot} yields a much larger quantity of broken bonds for a given Δ , indicating a much lower critical velocity (because of the noise in this lattice we cannot realize the zero microbranch regime). In addition, we check whether using larger-scale lattices ($f = 8$) yields the same fracture patterns. In Fig. 9(b) we can see that fracture patterns remain similar using the smaller value of α_{pot} (here we used the perturbed hexagonal lattice), though for a given Δ the microbranches are larger, as expected.

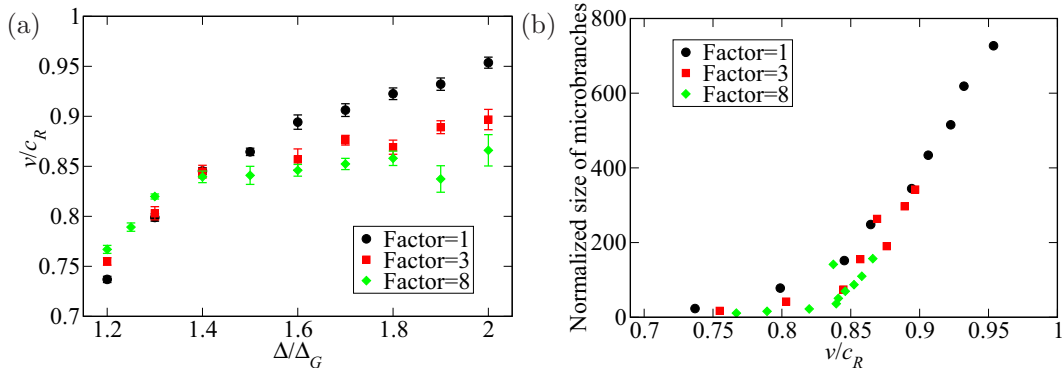


FIG. 8. (Color online) (a) The $v(\Delta)$ curve of a perturbed hexagonal lattice using different lattice sizes. (b) Total size of broken bonds in microbranches as a function of the crack velocity.

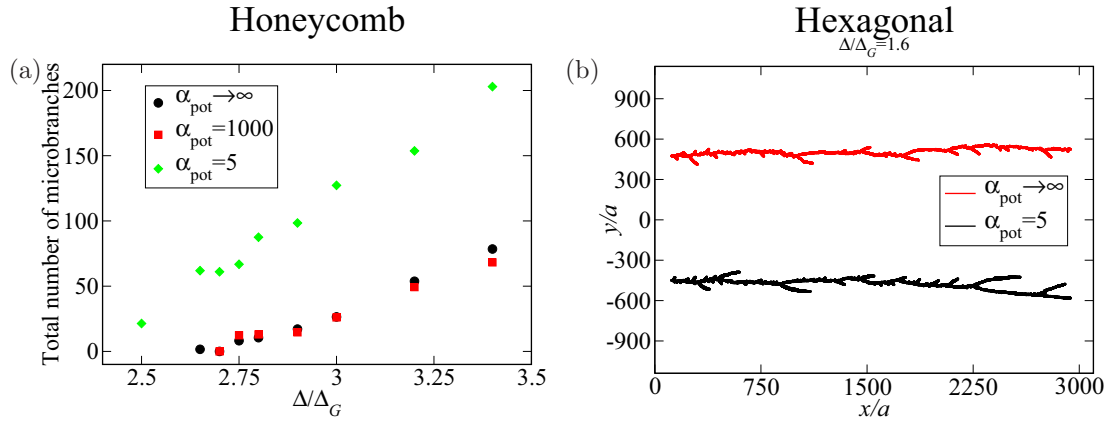


FIG. 9. (Color online) (a) The total size of microbranches as a function of the driving displacement Δ/Δ_G using different values of α_{pot} along with the piecewise linear model ($\alpha_{pot} \rightarrow \infty$) using perturbed honeycomb lattice with $f = 1$. (b) The microbranching pattern in a perturbed hexagonal lattice using larger-scale lattices ($f = 8$) for $\Delta/\Delta_G = 1.6$ and $\eta = 0.25$ for $\alpha_{pot} \rightarrow \infty$ in the upper curve and for $\alpha_{pot} = 5$ in the lower curve.

C. Microbranching statistics

Having larger systems enables, for the first time, the generation of enough statistics to examine important quantitative features of the microbranches that have been measured experimentally [1,5]. Since in this study we obviously are restricted to 2D features only, we focused here on the branching angle of the microbranches and on the power-law shape of the microbranches.

The experimental studies on PMMA finds a narrow distribution of the branching angle between $20^\circ \leq \theta \leq 40^\circ$, with

an average angle of 30° [5]. We note that a previous study using a random perturbed-Born-Maxwell model [40] yielded the wrong branching angle, namely 15° . In Fig. 10 we present the branching angle distribution of all the microbranches generated using all the values of Δ/Δ_G in the different models that were used in this study. We can see that in all the models studied, the average branching angle is near 30° , very much like the experimental branching angle. The variance is different using the different models, where the variance of the CRN lattice is the narrowest and thus most similar to the

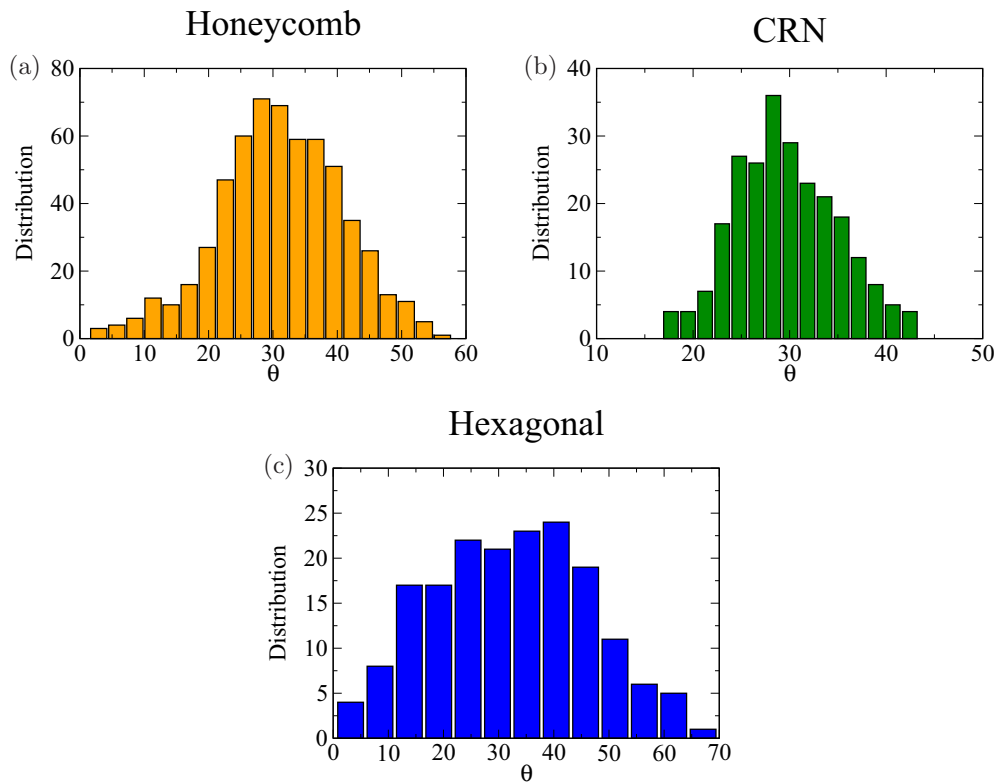


FIG. 10. (Color online) The distribution of the branching angle of the microbranches arising nearby the main crack using (a) a perturbed honeycomb lattice, (b) the CRN model, and (c) a perturbed hexagonal lattice.

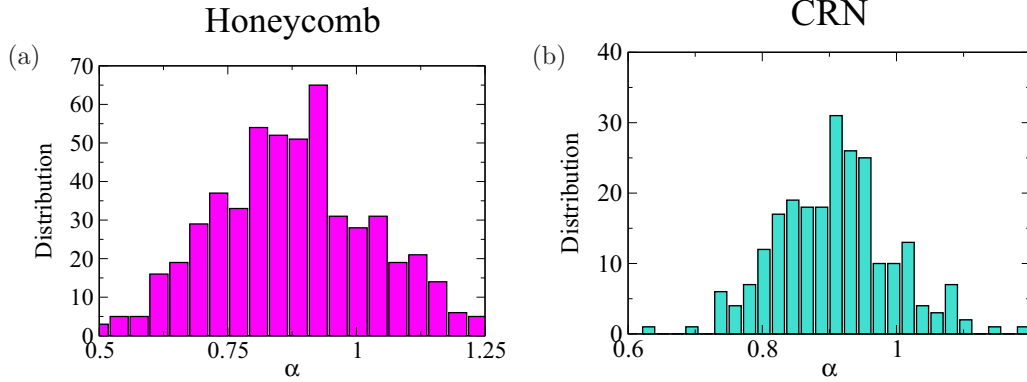


FIG. 11. (Color online) The distribution of the power of the power-law shaping of the microbranches arise nearby the main crack using (a) a perturbed honeycomb lattice and (b) the CRN model.

experiments. We also note that this result corresponds nicely with the LEFM microbranch analysis of Ref. [41], which yields a 27° branching angle.

One of the most striking features that was discovered in the experiments was a power-law shape of the branches, $y = ax^\alpha$ (x and y are the spatial coordinates of the microbranch such that $x = y = 0$ is the location of the “root” of the microbranch close to the main crack), with a universal power, $\alpha \approx 0.7$, for several different materials [1,5]. On the one hand, our previous studies using CRN or a perturbed honeycomb lattice yielded only straight ($\alpha \approx 1$) microbranches [13,25]. On the other hand, using a perturbed hexagonal lattice [13] we obtained branches that showed a power-law shape with $\alpha \approx 0.5$, though the results were noisy due to the relatively small number of broken bonds in each microbranch. We note that the LEFM analysis of Ref. [41] yields $\alpha = 2/3$, which is close to the experimental result, but this analysis assumes symmetric branching, when our branching (and the experimental results) is by no means symmetric. We also note that the branches seen in the elastic beam model [42] or the Born-Maxwell model [40] look very noisy, without a clear power-law shape. In this study, using larger lattices we can check the shape of the microbranches based on relatively large microbranches (≈ 100 broken bonds in each microbranch). In Figs. 11 and 12(a) we can see the power distribution for the different kinds of lattices.

We can clearly see that the maxima of all the distributions are around $\alpha \approx 0.85-0.9$, which is indeed less than 1 (straight lines). Looking closely at the larger lattices ($f = 9$) in Figs. 1 and 2 we can see the nonlinear power-law shape of the large branches, especially for the perturbed hexagonal lattice. In Fig. 12(b) we can see a scatter-plot of α as a function of the branch size for the perturbed hexagonal lattice case. It is clear that α converges on the value $\alpha \approx 0.7$ for the largest microbranches, which is close to the experimental value. The data for all three models is shown in Fig. 13. The other models do not show the decrease in α for the longest branches that is apparent for the hexagonal case, and perhaps data for longer microbranches are needed in the other cases, but in any case the asymptotic value of the exponent in all cases is less than unity.

V. DISCUSSION

We have used relatively large-lattice fracture simulations using GPU parallel computing [with $\mathcal{O}(5 \times 10^6)$ particles] for studying mode-I fracture. We find that the basic results from small lattices [$\mathcal{O}(5 \times 10^4)$ particles] are confirmed using the larger-size systems. The fracture patterns look more physical with a larger system, due to the large number of broken bonds in each microbranch. The width of the microbranch region relative to the system width decreases, a necessary condition

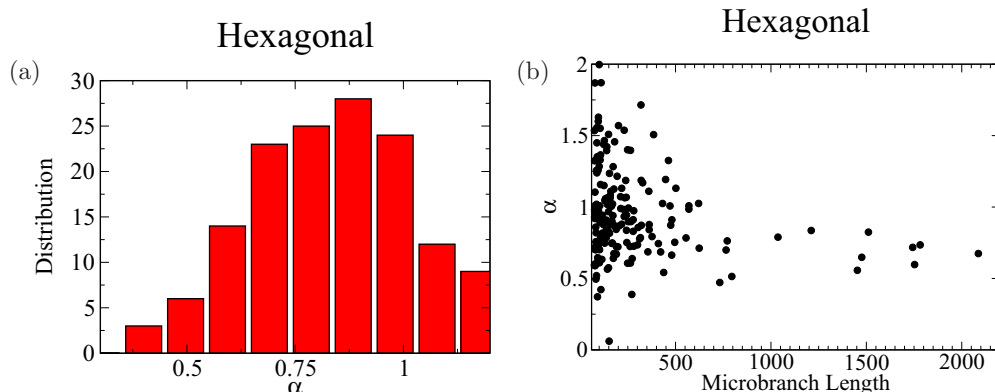


FIG. 12. (Color online) (a) The distribution of α , the power-law exponent ($y = ax^\alpha$) of the microbranches arising near the main crack for a perturbed hexagonal lattice. (b) A scatter-plot of the power α of the power-law exponent of the microbranches. We can clearly see that for the long branches, α converges on the value $\alpha \approx 0.7$, which is close to the experimental value.

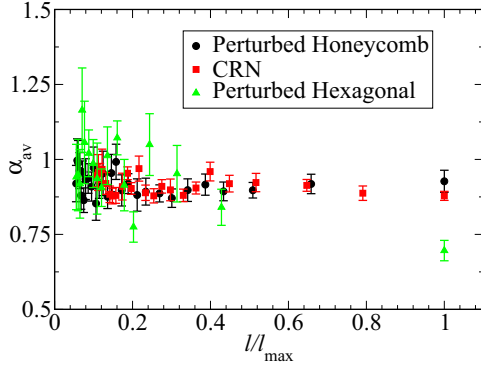


FIG. 13. (Color online) The distribution of α , the power-law exponent ($y = ax^\alpha$) of the microbranches arising near the main crack for the perturbed hexagonal, perturbed honeycomb, and CRN models, as a function of the microbranch length.

if these models are to be taken seriously. The basic properties of the microbranches, like the total length of the microbranches and the oscillations of the derivative of the electrical resistance with respect to the time-based velocity measurements, which were extremely noisy when using small lattices, look more smooth and realistic in the larger lattices. In particular, there is now a clearer transition between the regime of steady-state cracks, which there is a negligible amount of broken bonds beside the main crack, and the regime of instability, where the amount of broken bonds in the microbranches increases dramatically. The sharp transition is particularly clear in the hexagonal perturbed lattice [Fig. 8(b)].

In addition, important features of the microbranches that have been found and studied experimentally are recovered in our large system simulations. The correct branching angle is found, and in the CRN lattice the correct variance is also obtained. The universal power-law shape that was found in different experimental studies [5] is recovered here, and for the larger branches, we get the correct power in the hexagonal perturbed lattice.

In future work, we plan to exploit the power of GPU parallel computing to run 3D simulations using $\mathcal{O}(5 \times 10^6)$ particles,

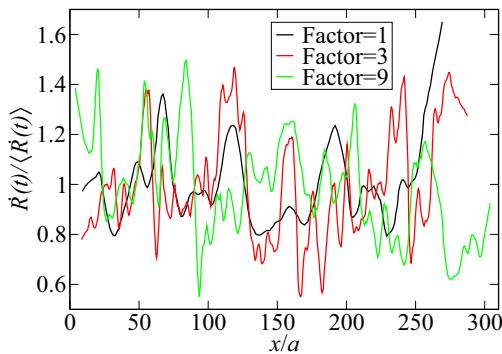


FIG. 14. (Color online) The derivative of the electrical resistance with respect to the time using a perturbed honeycomb lattice with $\Delta/\Delta_G = 3.4$ using the different lattice sizes. The plots are normalized in the x axis to the $f = 1$ size (i.e., the $f = 9$ results are divided by 9, etc.)

with the goal of studying the different aspects concerning the 3D nature of the microbranches. We intend to check the similarities and the differences between 2D and 3D mode-I fracture simulations and to find the regime when the 2D model is sufficient, and on the other hand, the regime where 3D simulations are crucial.

ACKNOWLEDGMENTS

S. I. Heizler and D. A. Kessler thank Jay Fineberg and his research group for useful advice and comments. S. I. Heizler thanks Oded Padon for helpful advice and lessons in using CUDA and GPU computing.

APPENDIX A: GPU-ACCELERATED C CODE

In this appendix we discuss implementation of our codes using CUDA and the run times of the CUDA runs using NVIDIA's Tesla C2050/C2070 GPU for the different modules that were used in this study and the acceleration ratios between a single CPU run and the GPU run. We rewrote our C codes and replaced the main time-demanding functions by CUDA kernels [37]. CUDA is a computer code language that was developed by NVIDIA for using its GPUs. We note that, in principle, one could use OpenCL, a general language for any GPU device, but CUDA is optimized for NVIDIA's graphic cards.

For using GPU computing optimally, the code should be written as a function of the particular hardware. Naively, the computational tasks are divided into several blocks, each block containing a specific number of threads, when the threads in the same block execute simultaneously. In this work we used 512 threads per block, which is the maximal number of threads per block available on our graphic card. The parameters of the physical problem are loaded to the *global memory* of the GPU and each thread computes one computational task, such as the force of one spring that acts on a pair of atoms. Such a naive choice, however, only produces up to a ten times acceleration, since there are a lot of calls to the global memory (which is relatively slow) for each atom calculating the force, especially in the three-body force law. Thus, we extensively employed the option of using *shared memory* (which is almost as fast as cache memory, shared for all the threads in the same block and limited to 64 K) to further accelerate the simulations, especially in the molecular-dynamics module [37,38]. The global memory of Tesla C2050/C2070 GPU is about 2.5 Gbytes, which is the limiting factor of the number of atoms in the simulation. In this work we used double-precision accuracy for all of our calculations (so using float precision will increase the number of atoms by a factor of 2, which is not significant; the main issue of this study is the effect of increasing the number of atoms by two orders of magnitude).

The underlying plan of the main, molecular dynamics, module using shared memory is to split the (potentially random, and thus general) grid of atoms to several physical zones (very much like Open-MPI as opposed to OpenMP parallelization) with lists that connect between the zones applied as a boundary condition for each physical zone; for the central elastic force law (and also for the viscoelastic force law) we sort the bonds, and for the three-body force law we sort the atoms. Each zone ("block" in the CUDA jargon) loads the locations and the velocities to a fast shared memory, and each

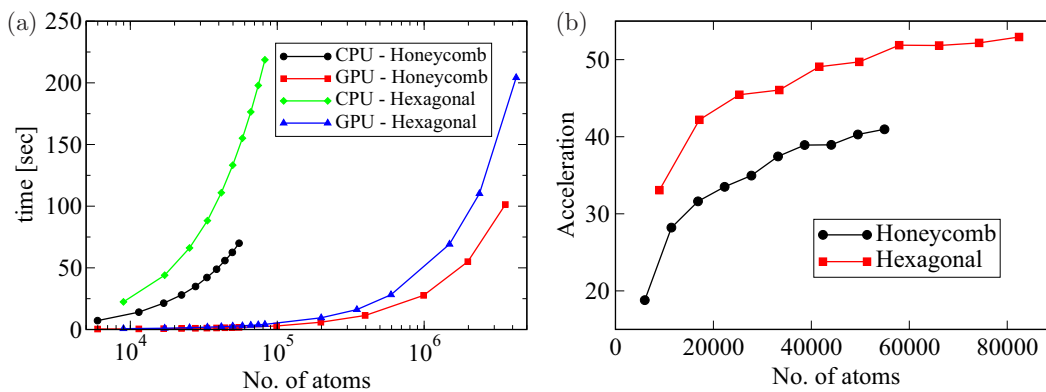


FIG. 15. (Color online) (a) Simulation times (in [sec]) of 1000 cycles of the molecular-dynamics Euler scheme as a function of the system size (both using honeycomb and hexagonal lattices) using unoptimized C code with CPU and with CUDA using GPU. (b) The acceleration run times between GPU and CPU as a function of the system size (for honeycomb and hexagonal lattices).

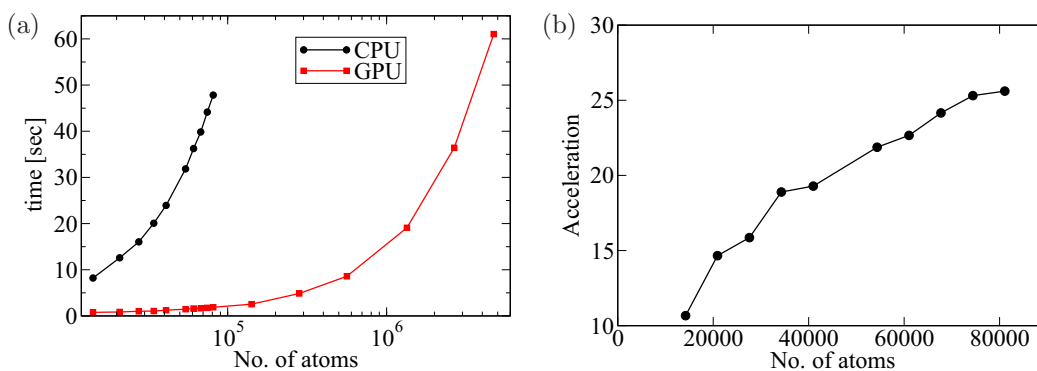


FIG. 16. (Color online) (a) Simulation times (in [sec]) for 1000 iterations of a Jacobi-method Laplace solver (for the electrical resistance) as a function of the system size using unoptimized C code with CPU and with CUDA using GPU (the times are similar also in Red-Black Gauss Seidel method). (b) The acceleration run times between GPU and CPU as a function of the system size.

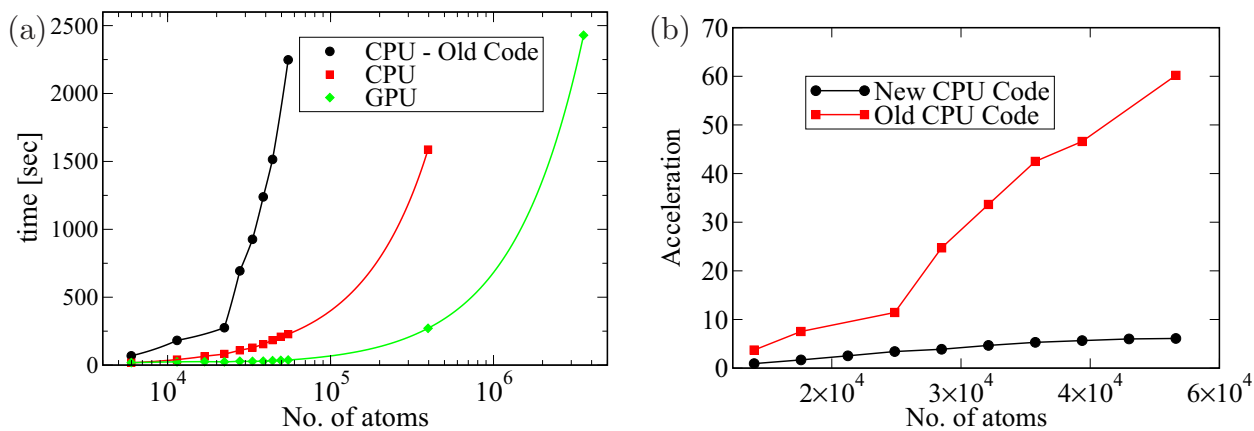


FIG. 17. (Color online) (a) Simulation times (in [sec]) for a WWW Monte Carlo scheme for producing a CRN (simulation stopped while the energy reaches half of the initial random energy) as a function of the system size using unoptimized C code with CPU, with CUDA using GPU and with the “old-CPU” code used in Ref. [25]. (b) The acceleration run times between GPU and CPU and the “old-CPU” codes as a function of the system size.

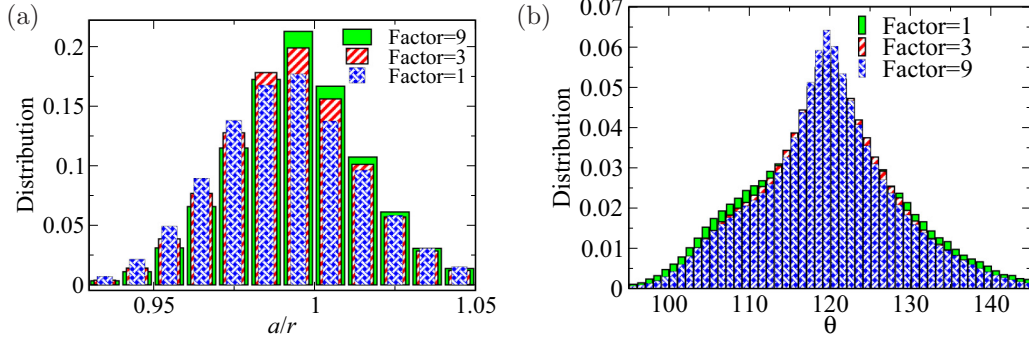


FIG. 18. (Color online) (a) The radial distance distribution of the bonds in CRN using different lattice sizes. (b) The angular distribution of the bonds in the CRN using different lattice sizes.

“thread” calculates the force of a certain bond (for the central force law) or atom (for the three-body force law). Thus, instead of several calls to the global memory for each atom’s location, the calls are for the fast shared memory, and so good efficiency is then achieved. Since the threads in the same block execute simultaneously, we have to use CUDA *atomic* commands to sum correctly the contribution of the forces exerted by the neighboring atoms. Then, the new velocities and locations are calculated by simple CUDA kernels.

The electrical resistance module is basically solving a nonlinear Laplace equation. We used the methodology that was introduced in Ref. [39] for calculating the electrical resistance (a constant grid of bonds with $\sigma = 1$), while a cracked bond in the molecular-dynamics module determines the “cracked” ($\sigma = 0$) bonds in the constant grid of the electrical resistance. Thus, we used the same well-known methodology of using the CUDA kernels for solving 2D diffusion equations [38], including the use of shared memory. We implemented both Jacobi and red-black gauss-Seidel methods of solution, but no significant difference (in terms of the number of iterations for convergence) was found between the methods. In Fig. 14 we can see an example of the derivative of the electrical resistance with respect to the time using a perturbed honeycomb lattice for a specific Δ/Δ_G . We can see that using different size lattices (using the new GPU code in the larger lattices and the CPU code in the smaller lattice), we can see that the shape of the curves of electrical resistance look very much like the experimental RMS amplitude of the crack velocity [5,6] (that is measured via the electrical resistance [25]).

The parallel Monte Carlo algorithm module for generating the CRN required extra care. Since the effect on the energy of each possible switch of bonds should be considered independently, each switch should be separate from all the other simultaneous possible switches (to avoid over-lapping of the switches and their neighboring zone). We mention that we use the parallel *THRUST* library (in CUDA) for sorting efficiently the nearest bonds for each bond, every given number of cycles.

In Figs. 15(a) and 16(a) we can see the typical run times for 1000 cycles (in seconds) for the molecular dynamics module and the Laplace solver module as a function of the system size. We can clearly see the benefit of using GPU computing, while the main benefit is the possibility to run systems with a large number of atoms, which with a single CPU was prohibitively

time-consuming. The run time using $\mathcal{O}(10^4)$ atoms with a single CPU is similar to the run time using $\mathcal{O}(10^6)$ atoms with a single GPU. In Figs. 15(b) and 16(b) we see the acceleration ratios between a single CPU and a single GPU (of course, only for small systems, when a CPU run is available). We can see the significant acceleration, 40 times faster for the honeycomb lattice and over 50 times faster for a hexagonal lattice due to the more demanding three-body force law. In the Laplace solver the speedup is a little bit lower and stands at approximately 25 times faster for the GPU versus a single CPU.

In Fig. 17 we can see the run times and the acceleration ratio using a single CPU and the GPU for the Monte-Carlo module. We can see here that the acceleration ratio is lower than in the previous modules (about $\approx 5-10$), but still, in larger lattices [$\mathcal{O}(10^6)$ atoms], the benefit is clear. We mention that since the programming using CUDA is much more demanding from the programmer, especially regarding the memory management, while reprogramming the code, we improved our old-CPU code (that was in use in Ref. [25]), significantly; the acceleration ratio of the GPU code to the old-CPU code is ≈ 60 .

APPENDIX B: CRN MONTE CARLO PARALLEL CUDA ALGORITHM

In previous work [25] we have shown that the CRN shares similar features with real amorphous matter, like amorphous

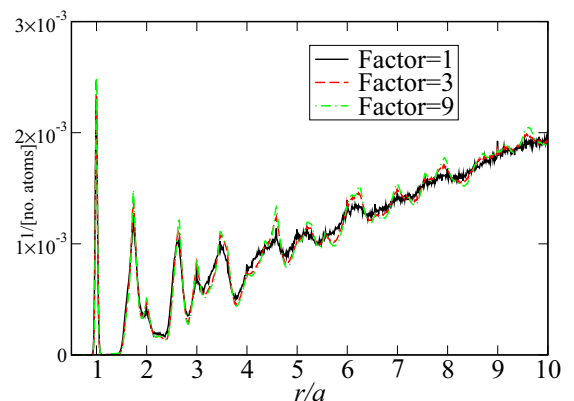


FIG. 19. (Color online) The radial distribution function [RDF or $g(r)$] of the CRN using different lattice sizes.

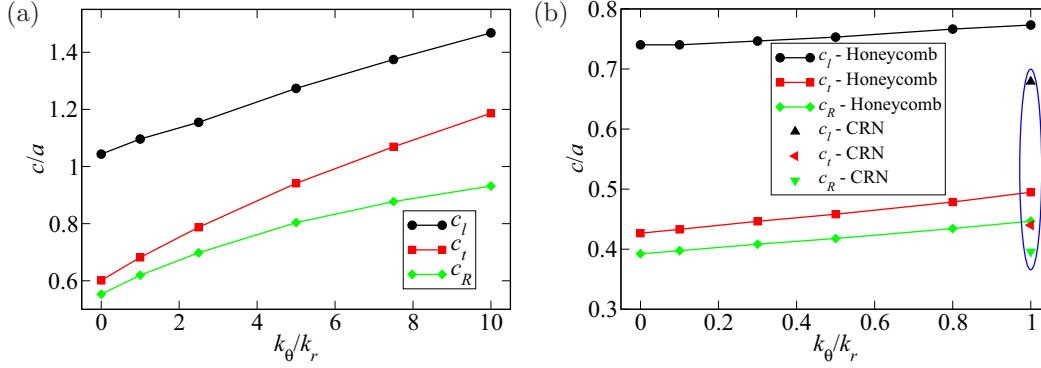


FIG. 20. (Color online) (a) The longitude and the transverse sound wave speeds along with the resulting calculated Rayleigh surface wave speed using Eq. (C1) for the hexagonal lattice as a function of k_θ/k_r . (b) The same in the honeycomb lattice. The sounds velocities for the CRN that was used in this paper ($k_\theta/k_r = 1$) are presented in the ellipse.

silicon [32]. In this appendix we check explicitly the quality of the parallel GPU algorithm, generating a CRN. In Fig. 18 we can see the radial and angular distributions of the bonds in the CRN using different lattice sizes, and in Fig. 19 we can see the radial distribution function $g(r)$ using different lattice sizes. $f = 1$ [of $\mathcal{O}(10^4)$ atoms] is the data using the old CPU code that was in use in Ref. [25], when larger lattices were produced via the new GPU algorithm.

We can see that the radial and angular distributions and the $g(r)$ curves are similar under the scaling of the lattice size (the number of the bonds or angles). This proves the validity of the parallel GPU algorithm, comparing the old CPU algorithm (that was verified before against experiments). Moreover, the RDF in the larger lattice size is smoother due to better statistics.

APPENDIX C: THE RAYLEIGH SURFACE WAVE SPEED WITH $k_\theta \neq 0$ LATTICES

Since the models in this paper use a three-body potential law (in addition to the central two-body force law) with $k_\theta \neq 0$, we need to recalculate the Rayleigh wave speed c_R , which is the terminal velocity for mode-I fracture [9] for different k_θ/k_r . The most convenient way to calculate the Rayleigh wave speed is to calculate first the longitude (primary) c_l and the transverse (secondary) c_t wave speeds and then to calculate the Rayleigh wave speed via the well-known formula [43]:

$$\left(1 - \frac{c_R^2}{c_t^2}\right)^2 - 4\left(1 - \frac{c_R^2}{c_l^2}\right)^{1/2} \left(1 - \frac{c_R^2}{c_t^2}\right)^{1/2} = 0. \quad (\text{C1})$$

For $k_\theta = 0$ the expressions for c_l and c_t , and thus also for c_R , can be derived analytically for a 2D hexagonal lattice with a as the lattice scale (for $k_r = m = 1$; the wave velocities scales as $\sqrt{k_r/m}$):

$$c_l^{\text{Hex}} = \frac{3}{\sqrt{8}}a, \quad c_t^{\text{Hex}} = \sqrt{\frac{3}{8}}a, \quad c_R^{\text{Hex}} = \frac{\sqrt{3 - \sqrt{3}}}{2}a, \quad (\text{C2})$$

and for a 2D honeycomb lattice:

$$c_l^{\text{Hon}} = \frac{3}{4}a, \quad c_t^{\text{Hon}} = \frac{\sqrt{3}}{4}a, \quad c_R^{\text{Hon}} = \frac{\sqrt{3 - \sqrt{3}}}{2\sqrt{2}}a. \quad (\text{C3})$$

We calculate c_l and c_t via measuring the wave velocities by initiating longitude and transverse small deformations in the end of the samples in the different lattices that we use in this study and then find c_R via Eq. (C1). The results are shown in Fig. 20(a) for the hexagonal lattice and in Fig. 20(b) for the honeycomb and CRN lattices.

We can see that for both lattices, the numerical value for the wave velocities using $k_\theta = 0$ reproduce the analytical values, Eqs. (C2) and (C3), respectively. In the hexagonal lattice using $k_\theta/k_r = 10$ (which was the value used in this study) the Rayleigh wave speed increases by $\approx 65\%$ relative to the $k_\theta = 0$ value. In the honeycomb lattice, where we use $k_\theta/k_r = 1$ at most, the Rayleigh wave speed increases by $\approx 12\%$ relative to the $k_\theta = 0$ value. We note the CRN speeds [in the ellipse in Fig. 20(b)] are a little bit slower than the pure honeycomb lattice. In addition we note that the random noise of the perturbed lattice changes the wave speeds less than 1%, and that the wave speeds are not affected at all by α_{pot} .

[1] J. Fineberg and M. Marder, *Phys. Rep.* **313**, 1 (1999).
[2] E. Bouchbinder, J. Fineberg, and M. Marder, *Annu. Rev. Condens. Matter Phys.* **1**, 371 (2010).
[3] E. Bouchbinder, T. Goldman, and J. Fineberg, *Rep. Progr. Phys.* **77**, 046501 (2014).
[4] J. Fineberg, S. P. Gross, M. Marder, and H. L. Swinney, *Phys. Rev. B* **45**, 5146 (1992).
[5] E. Sharon and J. Fineberg, *Phys. Rev. B* **54**, 7128 (1996).
[6] E. Sharon and J. Fineberg, *Adv. Eng. Mater.* **1**, 119 (1999).

[7] A. Livne, E. Bouchbinder, and J. Fineberg, *Phys. Rev. Lett.* **101**, 264301 (2008).
[8] M. Ramulu and A. S. Kobayashi, *Int. J. Fract.* **27**, 187 (1985).
[9] L. B. Freund, *Dynamic Fracture Mechanics* (Cambridge University Press, Cambridge, 1998).
[10] E. H. Yoffe, *Philos. Mag.* **42**, 739 (1951).
[11] J. D. Eshelby, in *Inelastic Behavior of Solids* (McGraw-Hill, New York, 1970), pp. 77–113.
[12] M. Adda-Bedia, *J. Mech. Phys. Solids* **53**, 227 (2005).

- [13] S. I. Heizler, D. A. Kessler, and Y. S. Elbaz, *Phys. Rev. E* **88**, 022401 (2013).
- [14] L. I. Slepyan, Dokl. Akad. Nauk SSSR **258**, 561 (1981) [Sov. Phys. Dokl. **26**, 538 (1981)]
- [15] Sh. A. Kulamekhtova, V. A. Saraikin, and L. I. Slepyan, Izv. Akad. Nauk SSSR Mekh. Tverd. Tela **19**, 112 (1984) [Mech. Solids **19**, 102 (1984)].
- [16] M. Marder and X. Liu, *Phys. Rev. Lett.* **71**, 2417 (1993).
- [17] D. A. Kessler and H. Levine, *Phys. Rev. E* **59**, 5154 (1999).
- [18] D. A. Kessler and H. Levine, *Phys. Rev. E* **63**, 016118 (2000).
- [19] L. Pechenik, H. Levine, and D. A. Kessler, *J. Mech. Phys. Solids* **50**, 583 (2002).
- [20] S. I. Heizler, D. A. Kessler, and H. Levine, *Phys. Rev. E* **66**, 016126 (2002).
- [21] S. I. Heizler and D. A. Kessler, *Contin. Mech. Thermodyn.* **22**, 505 (2010).
- [22] D. Holland and M. Marder, *Phys. Rev. Lett.* **80**, 746 (1998).
- [23] H. Gao, F. F. Abraham, and M. J. Buehler, *Nature* **426**, 141 (2003).
- [24] M. Marder and J. Fineberg, *Phys. Today* **49**, 24 (1996).
- [25] S. I. Heizler, D. A. Kessler, and H. Levine, *Phys. Rev. E* **84**, 026102 (2011).
- [26] W. H. Zachariassen, *J. Am. Chem. Soc.* **54**, 3841 (1932).
- [27] F. Wooten, K. Winer, and D. Weaire, *Phys. Rev. Lett.* **54**, 1392 (1985).
- [28] F. Wooten and D. Weaire, in *Solid State Physics* (Academic Press, New York, 1987), Vol. 40, p. 1.
- [29] P. Y. Huang, S. Kurasch, A. Srivastava, V. Skakalova, J. Kotakoski, A. V. Krasheninnikov, R. Hovden, Q. Mao, J. C. Meyer, J. Smet, D. A. Muller, and U. Kaiser, *Nano Lett.* **12**, 1081 (2012).
- [30] F. R. Eder, J. Kotakoski, U. Kaiser, and J. C. Meyer, *Sci. Rep.* **4**, 4060 (2014).
- [31] A. Livne, G. Cohen, and J. Fineberg, *Phys. Rev. Lett.* **94**, 224301 (2005).
- [32] K. Laaziri, S. Kycia, S. Roorda, M. Chicoine, J. L. Robertson, J. Wang, and S. C. Moss, *Phys. Rev. Lett.* **82**, 3460 (1999).
- [33] Y. Tu, J. Tersoff, G. Grinstein, and D. Vanderbilt, *Phys. Rev. Lett.* **81**, 4899 (1998).
- [34] G. N. Hassold and D. J. Srolovitz, *Phys. Rev. B* **39**, 9273 (1989).
- [35] L. Monette and M. P. Anderson, *Model. Simul. Mater. Sci. Eng.* **2**, 53 (1994).
- [36] H. Gao, Y. Huang, and F. F. Abraham, *J. Mech. Phys. Solids* **49**, 2113 (2001).
- [37] O. Padon, *Trends in Scientific Computing and GPU Computing* (in Hebrew), Physics Department, Nuclear Research Center-Negev, N-11/010 (2011).
- [38] C. Cooper, *GPU Computing with CUDA*, UTFSM, Valparaíso, Chile (Boston University Lecture Notes, August, 2011).
- [39] D. Bonamy and K. Ravi-Chandar, *Int. J. Frac.* **134**, 1 (2005).
- [40] P. Heino and K. Kaski, *Phys. Rev. E* **56**, 4364 (1997).
- [41] E. Katzav, M. Adda-Bedia, and R. Arias, *Int. J. Frac.* **143**, 245 (2007).
- [42] J. Åström and J. Timonen, *Phys. Rev. B* **54**, R9585 (1996).
- [43] J. D. Achenbach, *Wave Propagation in Elastic Solids* (North-Holland Publishing Company, Amsterdam, 1973).